electronics

Article

Energy Management Strategy for PEM Fuel Cell Hybrid Power System Considering DC Bus Voltage Regulation

Hoai-An Trinh, Van-Du Phan, Hoai-Vu-Anh Truong and Kyoung Kwan Ahn *

Department of Mechanical Engineering, University of Ulsan, Daehakro 93, Nam-gu, Ulsan 44610, Korea
* Correspondence: kkahn@ulsan.ac.kr; Tel.: +82-52-259-2282

Abstract: Developing an energy management strategy (EMS) is an important requirement to satisfy the load power demand for a proton-exchange membrane fuel cell (PEMFC) hybrid system under different working conditions. For this objective, this paper proposes an EMS to control the power distribution between the PEMFC, battery (BAT), and supercapacitor (SC) and regulate the DC bus voltage for matching the load power demand. In this strategy, fuzzy logic rules (FLRs) and low-pass filters (LPFs) are utilized to determine the reference currents for energy sources based on their dynamic response. In addition, current and voltage control loops are designed to provide the appropriate gains for compensators that can maintain a stable voltage on the DC bus. Finally, simulations are conducted in the MATLAB/Simulink environment to validate and compare the effectiveness of the proposed strategy with others. The simulation results present that the proposed EMS achieves the highest distributed power accuracy with an error of $(-2.1 \rightarrow 2.6)$ W, while reducing the DC bus voltage ripple by 1% under various load working conditions in comparison to the other approaches.

Keywords: hybrid power system; energy management strategy; PEMFC; fuzzy logic rules; DC bus voltage regulation

check for updates

Citation: Trinh, H.-A.; Phan, V.-D.; Truong, H.-V.-A.; Ahn, K.K. Energy Management Strategy for PEM Fuel Cell Hybrid Power System Considering DC Bus Voltage Regulation. *Electronics* **2022**, *11*, 2722. https://doi.org/10.3390/electronics11172722

Academic Editor: Raffaele Carli

Received: 30 July 2022
Accepted: 25 August 2022
Published: 30 August 2022

1. Introduction

The development of renewable energy sources is quickly becoming an indispensable solution for inhibiting environmental pollution caused by types of machines or power generation systems that consume fossil fuels [1,2]. As a result, power sources such as solar, wind, or fuel cell are regarded as economically feasible renewable sources for multiple applications. These energy sources are used as a primary source to serve the load power demand. Recently, the PEMFC has gained attention as a major and viable contender to take the place of traditional energy storage systems (ESSs) such as BAT or SC [3]. Moreover, it is also distinguished by its lower operating temperatures, better power density, and higher energy conversion compared to other types of fuel cells [4]. However, variable nature characteristics such as a slow response and inability to satisfy abrupt load demands and absorb regenerative energy are existing obstacles when employing standalone PEMFC. Hence, the PEMFC system is highly dependent on an ESS to provide power delivery to load continuity with a fluctuating power source. As a result, various researchers studied the combination of BAT-SC with PEMFC. The hybrid systems of PEMFC-BAT-SC have been used in a variety of research fields including DC microgrids [5–7], hybrid electric vehicles [8–10], construction machinery [11,12], hybrid tramway powertrains [13–15], and so on. The aforementioned literature showed that this hybrid configuration could yield an improved performance, decrease system size, address the issue of fuel economy, and increase device longevity. However, in order to achieve high operating effectiveness for a complicated hybrid power system (HPS), the EMS should be designed to properly manage power distribution from energy sources to the powertrain.

In the literature, many energy management methods have been reported to control the HPS. In [16], a distributed energy management system was constructed for the HPS based on a rule-based power distribution strategy. By using the charge and discharge limitations of power capability and residual capacity, the presented EMS might increase the lifespan and enhance the economics of the hybrid energy storage system. Similar to [17–19], rule-based EMSs were also developed for the fuel cell electric vehicle (FCEV) to determine the required power of electrical sources and obtain fuel economy by regulating the power distribution of BAT and SC through charge and discharge mechanisms. To minimize hydrogen consumption and extend the life of system components, Kaya et al. [20] proposed two control strategies based on the simplicity of their structure and characteristics, which may be readily applied to the many types of FCEVs. These strategies have only been verified in two separate road models, the "stop-go road model" and the "uphill-downhill road model", and more complicated road models should be done for further research. For the fuel cell hybrid excavator, Do et al. presented an EMS in [21], to properly manage the power distribution of energy sources based on load power demand and increase the power performance under various operating scenarios. To improve the efficiency of a hybrid tramway system, Qi Li et al. [22,23] developed a state machine technique based on droop management to coordinate numerous power sources when load states changed. In [24], a simple control system was designed for a switcher locomotive-powered PEMFC-BAT-SC hybrid system to manage the power flows and load power demand levels while maintaining the proper state of charge (SOC) on the ESSs. In [25,26], Garcia et al. proposed an operational mode control and cascade control loop that could allocate the load power demand for each energy source, ensuring power performance and satisfying the hybrid tramway system's drive cycle under varying operating circumstances. According to the results of the aforementioned studies, these EMSs could ensure the HPS's overall efficiency and fulfill the load power demand. However, the switching modes of the rule-based mechanisms, which were frequently dependent on the on/off mechanism to control the specific working conditions, still remained the drawback of not offering a flexible operation and instability for the charge and discharge of ESSs.

By dealing with model uncertainty and complex decisions, FLRs have been applied in several studies for HPS's control strategies and energy management to determine the power distribution between the primary source and the ESS, while guaranteeing the system operated in a high-efficiency or fuel economy mode. In [5], Fagundes et al. proposed a fuzzy controller for energy management in the hybrid system of fuel cells and energy storage units. This approach was suitable for compensating/absorbing power during load transients, minimizing fuel cell stack damages, and balancing the SoC status of ESS through the charging/discharging process. For FCEV, in [27,28], FLRs and flatness control were combined to split the energy flow between three electrical sources. This strategy gained high efficiency in power-sharing from energy sources to satisfy the load power demand in different operating modes. To protect BAT from overcharging, a real-time fuzzy logic was described by Hemi et al. in [29] for three configurations of FCEV. The simulation results confirmed that the proposed strategy could satisfy the load power demand with the unknown driving cycles and achieve power distribution among energy sources. In [30,31], fuzzy-based EMSs were exploited for integrated PEMFC-BATs-SCs to improve the hybrid vehicle behaviors, enhance system efficiency, and prolong the component lifespan. For the fuel cell excavator system, Truong et al. [32] used the fuzzy-based EMS to maintain the load power demand, minimize fuel economy, and ensure the SOC of ESS. Using the same object, Dao et al. [33] introduced a combination of fuzzy-based EMS and optimal techniques to update the fuzzy membership functions (MFs) to save fuel consumption while improving system performance. In addition, depending on the different characteristics of power sources, the frequency decomposition techniques were applied to regulate the dynamic response, improve the power-sharing accuracy, and extend the lifetime of devices. Based on the Ragone diagram, LPFs were used in [34,35] to decompose the frequency ranges allowed by each power source, and improve the power performance of HPS while reducing stress and power fluctuation on the PEMFC and ESS. To achieve the optimum distribution of energy between the sources, Snoussi et al. [36] proposed an adaptive filtering-based EMS for minimizing hydrogen consumption and maintaining the constraints of each device, such as the permissible limitation of storage system capacities and battery current variation. According to the presented studies, the fuzzy logic technique and frequency decomposition approach performed well for power distribution between the PEMFC and ESS in the hybrid system. In [37], an EMS with the combination of FLRs and the frequency decoupling method using FPFs was proposed for HPS to achieve the appropriate power distribution and maintain a stable DC output voltage. However, the controllers of DC-DC converters in HPS were designed by the trial and error method without investigating the dynamic characteristics of these converters. As a result, it is difficult to identify suitable compensator gains. This can result in a shortage of supplied power for the load, especially if the required power varies abruptly. Therefore, the development of an EMS considering the design of the controller gains for DC-DC converters is required to achieve the overall system qualification and improve the stable DC bus voltage delivered to the load under different working conditions.

Motivated by the above analyses and the significant extension of the conference paper [37], this paper proposed an energy control strategy to guarantee energy performance and fuel economy, and improve the stability of the DC bus voltage for an HPS. The main contributions of the proposed control strategy are as follows: Firstly, FLRs are designed to determine an appropriate reference PEMFC power to supply the traction load by using the SOC of BAT and the load power demand. Secondly, the combination of FLRs and filtering-based methods are mainly utilized to ensure the proper power distribution of each energy source based on their dynamic characteristics and operating frequency ranges. Thirdly, the dynamics and response of converters are analyzed using the Bode diagram to produce the correct gains for compensators of current and voltage control loops that maintain the stability of the DC bus voltage based on the BAT. Finally, comparison results between the proposed strategy and other approaches are discussed to evaluate the effectiveness.

The rest of this paper is organized as follows: the configuration of HPS is described in Section 2. In Section 3, the energy control strategy is introduced. Simulation results are given in Section 4 to validate the effectiveness of the proposed strategy. Finally, the conclusions of this paper are presented in Section 5.

2. Configuration of Hybrid Power System

2.1. System Configuration

The proposed hybrid power topology is described in Figure 1 [37]. This hybrid system consists of a PEMFC as the primary energy source and an ESS that composes the lithium-ion BAT and SC bank. Two bidirectional and one unidirectional boost DC-DC converters are implemented to connect three power sources and the DC bus in parallel. These devices can supply the energy to the traction motor through an inverter based on the discharge or charge modes during the load variations. In order to overcome the mentioned problems when using standalone PEMFC, the ESS, with a high energy density and high power density, is utilized to supplement the lacking power in the initial phase, the transient period, peak power demands, or regenerative energy. It can be seen that this configuration provides a flexible mechanism for controlling the DC bus voltage, enhancing working performance, and achieving fuel economy for the PEMFC system.

2.2. PEMFC Model

In this work, the PEMFC Horizon H-200 200 W/24 V is used as the main power source for the hybrid system. To reproduce its characteristics, a detailed model in [38] is applied to construct the simulation model for the PEMFC that composes a stack module, auxiliary components of hydrogen and air supplying, water-cooling circulation, humidification, while neglecting the reactant flow inside the electrode. In this model, system parameters can be easily set up from the datasheet or by using the simple polarization curve of the testing process. The equivalent circuit of the PEMFC stack is described in Figure 2.

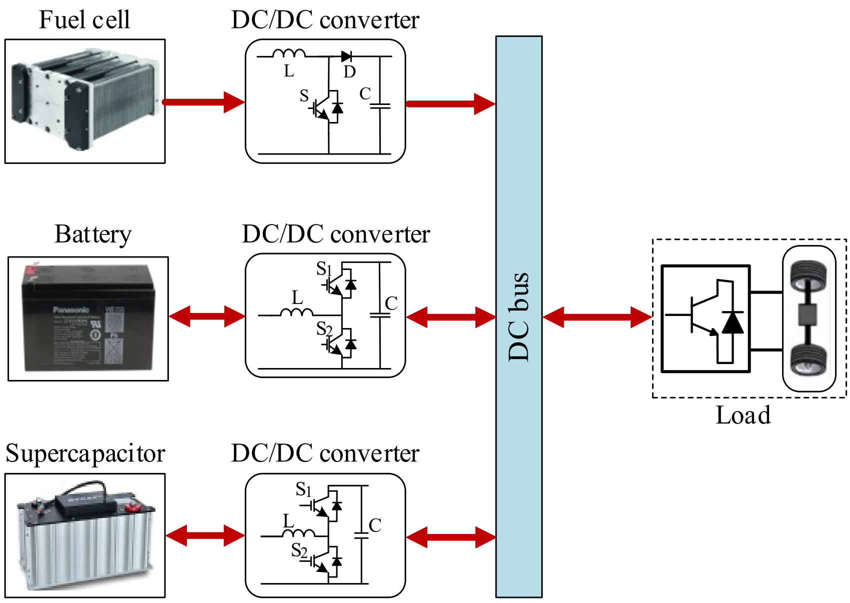

Figure 1. The PEMFC hybrid power system configuration [37].

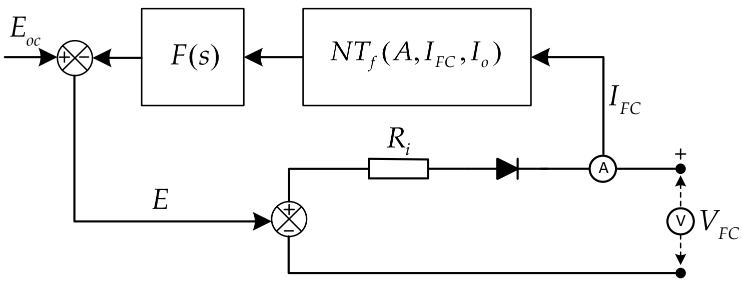

Figure 2. The detailed model of the PEMFC stack.

The output voltage of the PEMFC stack can be expressed as follows [38]:

$$V_{FC} = E - R_i I_{FC} \tag{1}$$

$$E = E_{oc} - F(s)NT_f(A, I_{FC}, I_o) = E_{oc} - NA\ln\left(\frac{I_{FC}}{I_o}\right)\frac{1}{\frac{T_d}{3}s+1} \tag{2}$$

where V_{FC} is the PEMFC stack voltage (V), E is the voltage source (V), R_i denotes the internal resistance (Ω), I_{FC} describes the PEMFC stack current (A), E_{oc} is the open-circuit voltage (V), N is the number of cells, A is the Tafel slope (V), I_o denotes the exchange current (A), and T_d presents the response time (s).

In the detailed PEMFC model, the Tafel slope, exchange current, and open-circuit voltage parameters are determined based on the variations of the input pressures, gas compositions, stack temperature, and flow rate of fuel and air. The open-circuit voltage is described by Equation (3):

$$E_{oc} = K_c E_n \tag{3}$$

where K_c is the voltage constant at the nominal condition of operation and E_n denotes the Nest voltage (V).

The Nest voltage is determined as follows:

$$E_n = \begin{cases} 1.229 + (T - 298)\frac{-44.43}{zF} + \frac{RT}{zF}\ln\left(P_{H_2}P_{O_2}^{\frac{1}{2}}\right) & ,T \leq 273\,^\circ K \\ 1.229 + (T - 298)\frac{-44.43}{zF} + \frac{RT}{zF}\ln\left(\frac{P_{H_2}P_{O_2}^{\frac{1}{2}}}{P_{H_2O}}\right) & ,T > 273\,^\circ K \end{cases} \tag{4}$$

where T is the operation temperature (°K), z denotes the number of moving electrons, R is the ideal gas constant (J/(mol °K)), F is the Faraday constant (A s/mol), P_{H_2} is the partial pressure of hydrogen inside the stack (atm), P_{O_2} is the partial pressure of oxygen inside the stack (atm), and P_{H_2O} is the partial pressure of water vapor (atm).

The partial pressure values are given by equations:

$$P_{H_2} = \left(1 - U_{f_{H_2}}\right)xP_{fuel} \tag{5}$$

$$P_{O_2} = \left(1 - U_{f_{O_2}}\right)yP_{air} \tag{6}$$

$$P_{H_2O} = \left(w + 2yU_{f_{O_2}}\right)yP_{air} \tag{7}$$

where $U_{f_{H_2}}$ is the rate of hydrogen utilization, $U_{f_{O_2}}$ denotes the rate of oxygen utilization, x is the percentage of hydrogen in the fuel (%), y is the percentage of oxygen in the oxidant (%), w is the percentage of water vapor in the oxidant (%), P_{air} is the absolute supply pressure of air (bar), and P_{fuel} is the absolute supply pressure of fuel (bar). Herein, the terms of $U_{f_{H_2}}$ and $U_{f_{O_2}}$ are defined as follows:

$$U_{f_{H_2}} = \frac{60000RTI_{FC}}{zFP_{fuel}V_{fuel}x} \tag{8}$$

$$U_{f_{O_2}} = \frac{60000RTI_{FC}}{2zFP_{air}V_{air}y} \tag{9}$$

where V_{fuel} is the fuel flow rate (lpm) and V_{air} is the air flow rate (lpm).

In Equation (2), the Tafel slope and exchange current are described as follows:

$$I_0 = \frac{zFk\left(P_{H_2} + P_{O_2}\right)}{Rh}\exp\left(\frac{-\Delta G}{RT}\right) \tag{10}$$

$$A = \frac{RT}{z\alpha F} \tag{11}$$

where k is the Boltzmann's constant (J/°K), α is the charge transfer coefficient, h is the Planck's constant (J s), and ΔG is the activation energy barrier (J/mol).

The output power of the PEMFC stack is formulated by:

$$P_{FC} = \eta V_{FC}I_{FC} \tag{12}$$

where P_{FC} is the output power (W) and η denotes the efficiency of the PEMFC stack.

The PEMFC parameters are given in Table 1.

Based on the technical specification of the PEMFC stack, the predetermined polarization curves of power–current (P-I) and voltage–current (U-I) are shown in Figure 3.

2.3. Battery Model

Due to its high energy density, fast dynamic response, and low self-discharge rate, the lithium-ion battery is a promising device that can be used to compensate for the lack of PEMFC power and store regenerative energy in the hybrid system. To explore its behaviors, an equivalent circuit is employed to construct the simulation model for the BAT, as shown in Figure 4.

Table 1. Parameters of the PEMFC model.

Parameter	Value	Parameter	Value
N	40	w	1%
R_i	1.0375 (Ω)	P_{air}	2 (bar)
T_d	7 s	P_{fuel}	0.5 (bar)
R	8.3145 (J/(mol °K))	V_{air}	2.6 (lpm)
z	2	V_{fuel}	6.452 (lpm)
F	96,485 (A s/mol)	k	1.38×10^{-23} (J/°K)
T	318 (°K)	α	1.2518
x	99.95 (%)	h	6.626×10^{-34} (J s)
y	50 (%)	η	40%

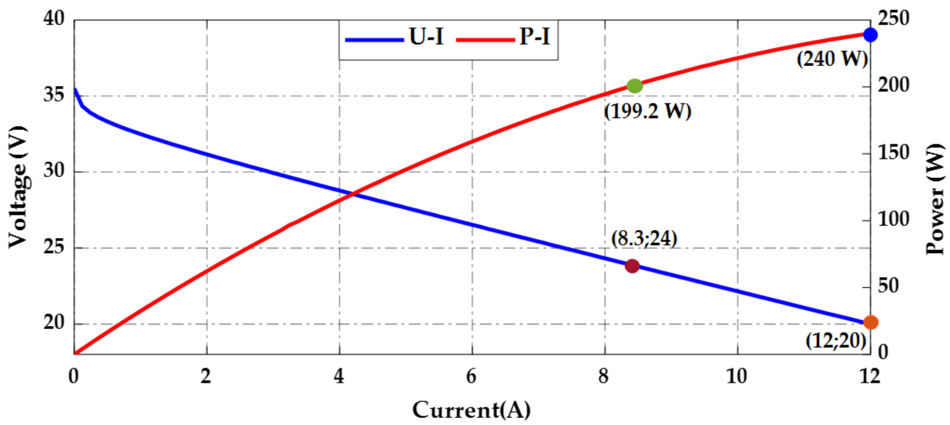

Figure 3. Polarization curves of the PEMFC stack.

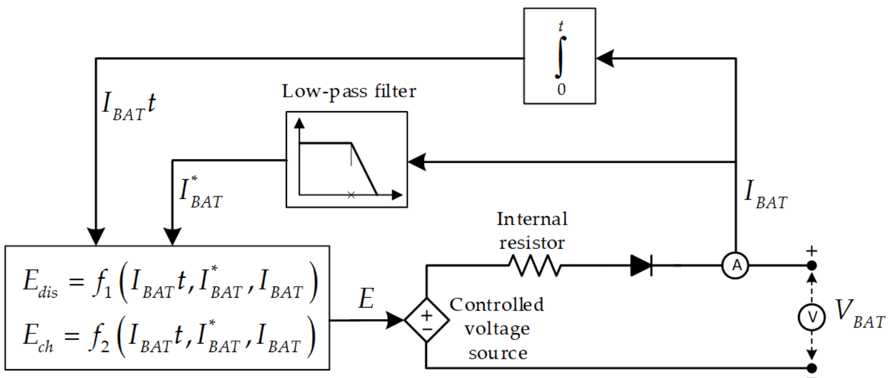

Figure 4. BAT model.

Depending on the discharge or charge mode, the nonlinear voltage is regulated to maintain the BAT's capacity in a reasonable performance. The voltage in the discharge mode is calculated as follows [39]:

$$\begin{aligned} E_{dis} &= f_1\left(I_{BAT}t, I^*_{BAT}, I_{BAT}\right) \\ &= E_0 - K\frac{Q}{Q-\int_0^t I_{BAT}dt}\cdot I^*_{BAT} - K\frac{Q}{Q-\int_0^t I_{BAT}dt}\int_0^t I_{BAT}dt + A_b \exp\left(-B\cdot\int_0^t I_{BAT}dt\right) \end{aligned} \tag{13}$$

where E_{dis} is the nonlinear voltage in discharge mode (V), E_0 is the BAT constant voltage (V), Q is the maximum BAT capacity (Ah), I_{BAT} is the BAT output current (A), I^*_{BAT} is the low-frequency current dynamics (A), K is the polarization constant (V/Ah), A_b is the exponential voltage (V), and B is the exponential capacity (Ah^{-1}).

For the charge mode, due to the fast increasing voltage of the BAT, the polarization resistance $K\left(Q/\left(Q-\int_0^t I_{BAT}t\right)\right)$ is regulated to depict the performance at the end of the charging process. Thus, the voltage is given by [39]:

$$\begin{aligned} E_{ch} &= f_2\left(I_{BAT}t, I^*_{BAT}, I_{BAT}\right) \\ &= E_0 - K\frac{Q}{\int_0^t I_{BAT}dt - 0.1Q}\cdot I^*_{BAT} - K\frac{Q}{Q-\int_0^t I_{BAT}dt}\int_0^t I_{BAT}dt + A_b\exp\left(-B\cdot\int_0^t I_{BAT}dt\right) \end{aligned} \tag{14}$$

where E_{ch} is the nonlinear voltage in charge mode (V).

The output voltage of the BAT model is represented as follows:

$$V_{BAT} = E_b - R_{\text{int}}I_{BAT} \tag{15}$$

where R_{int} is the BAT internal resistance (Ω), and E_b is the nonlinear voltage (V) that equals E_{dis} in discharge mode and equals E_{ch} in charge mode, as defined in Equations (14) and (15).

In addition, the SOC of the BAT (SOC_{BAT}) can be obtained from the current charge and the maximum capacity by:

$$SOC_{BAT}(t) = SOC_{BAT}(t_0) - \frac{1}{Q}\int_{t_0}^{t} I_{BAT}dt \tag{16}$$

where SOC_{BAT} is the SOC of the BAT (%), t is the instant time, and t_0 is the initial time.

A pack of six series and four parallels Panasonic NCR18650BF to create a lithium-ion BAT 21.6 V/12.8 Ah is used for the hybrid system. Its parameters are given in Table 2.

Table 2. Parameters of the BAT model.

Parameter	Value	Parameter	Value
E_0	23.4222 (V)	A_b	1.8139 (V)
Q	13.4 (Ah)	B	4.7705 (Ah^{-1})
K	0.012642 (V/Ah)	R_{int}	16.875 (mΩ)

From the input parameters, the polarization curves of the BAT model are shown in Figure 5.

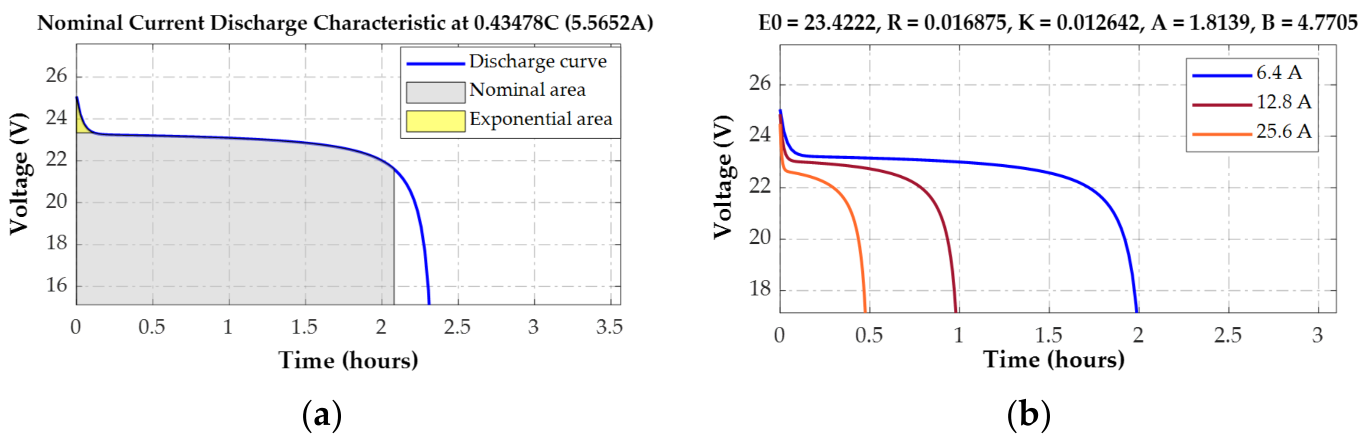

Figure 5. Polarization curves of the BAT. (**a**) Nominal current discharge characteristics. (**b**) Discharge current.

2.4. Supercapacitor Model

The SC is known as an electronic component with a fast dynamic response and high power density. In the hybrid system, it can be used to store the regenerative energy or release more energy to compensate for the peak power during the abrupt load variation. In this work, an SC model is constructed by using the Stern model [40–42]. The equivalent circuit of the SC model is illustrated in Figure 6.

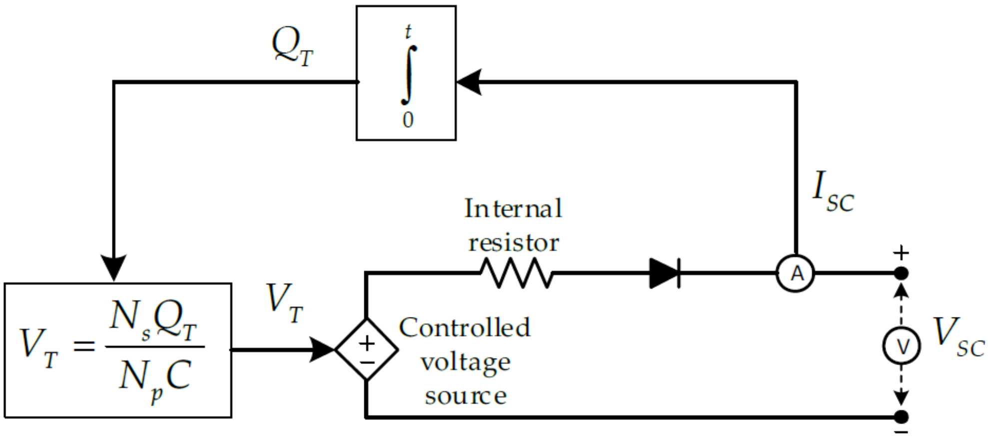

Figure 6. SC model.

The SC output voltage can be given by:

$$V_{SC} = \frac{N_s Q_T}{N_p C} - R_{SC} I_{SC} \tag{17}$$

where Q_T is the total electric charge (C), C is the capacitance of an electric double-layer capacitors cell (F), N_s denotes the cells in series, N_p presents cells in parallel, I_{SC} is the SC current (A), and R_{SC} is the internal resistance (Ω).

The capacitance of a cell can be expressed as

$$C = \left(\frac{1}{C_H} + \frac{1}{C_{GC}}\right)^{-1} \tag{18}$$

with

$$C_H = \frac{N_e \varepsilon \varepsilon_0 A_i}{d} \tag{19}$$

$$C_{GC} = \frac{F Q_c}{2 N_e R T} \sin\left(\frac{Q_c}{N_e^2 A_i \sqrt{8RT\varepsilon\varepsilon_0 c}}\right) \tag{20}$$

where C_H is the Helmholtz capacitance (F), C_{GC} is the Gouy–Chapman capacitance (F), N_e is the number of layers of electrodes, ε and ε_0 are the permittivity of material and free space (F/m), A_i is the interfacial area between electrodes and electrolyte (m^2), d is the molecular radius (m), F is the Faraday constant (A s/mol), R is the ideal gas constant (J/(mol °K)), Q_c is the cell electric charge (C), T is the operating temperature (°K), and c is the molar concentration (mol/m^{-3}).

Next, the total electric charge is defined by:

$$Q_T = \int_{t_0}^{t} I_{SC} dt \tag{21}$$

In addition, the SOC of the SC can be estimated through the output current and maximum capacity as follows:

$$SOC_{SC}(t) = SOC_{SC}(t_0) - \frac{1}{Q_{SC}}\int_{t_0}^{t} I_{SC}dt \tag{22}$$

where SOC_{SC} is the SOC of SC (%), Q_{SC} is the maximum SC capacity (Ah), t is the instant time, and t_0 is the initial time.

In this work, a supercapacitor bank of nine series cells of the Maxwell 450 F/2.7 V is used. Its parameters are given in Table 3.

Table 3. Parameters of the SC model.

Parameter	Value	Parameter	Value
N_s	9	N_e	1
N_p	1	d	10^{-9} (m)
R_{SC}	2.8 (mΩ)	ε	6.0208×10^{-10} (F/m)
T	298 (°K)	ε_0	8.85×10^{-12}(F/m)
F	96,485 (A s/mol)	Q_c	9 (C)
R	8.3145 (J/(mol °K))	c	208 (mol/m^{-3})

2.5. DC/DC Converter Models

In the hybrid power system, DC/DC converters are critical in controlling the required power from the energy sources for adapting to load power demand and keeping the DC bus voltage at the desired value. These converters are utilized in this study to connect the three energy sources of PEMFC, BAT, and SC with a DC bus that supplies voltage and current to the traction load. Depending on the role and function of each energy source, converters will operate to boost or buck the voltage that delivers to the DC bus through discharge or charge mechanisms. In detail, the boost converter is used to convert the lower voltage of the PEMFC to the higher voltage on the DC bus, whereas the buck–boost converters (bidirectional converters) are used to transform the voltage in two directions between BAT/SC and the DC bus, with the boost mode for discharging and the buck mode for charging. The structure of the DC/DC converters is described in Figure 7.

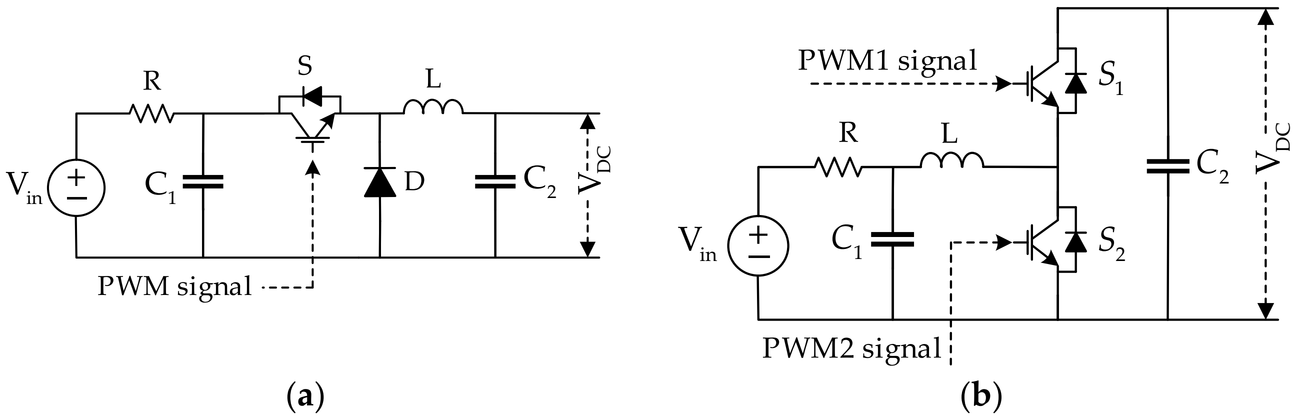

Figure 7. Structure of DC/DC converters. (**a**) Boost converter. (**b**) Buck–boost converter.

In Figure 7, the switching model is applied to build the structure of the DC/DC converters. The advantage of this model is that it can observe the switching actions, switching harmonics, and losses of switching components and investigate the converter dynamics. This model is mostly utilized for experimental applications, and an adaptive control loop is designed to generate the PWM signals for controlling the switching components.

Thus, the duty cycles are calculated to define the PWM signals for the DC/DC converters according to the reference current in the buck mode or boost mode. These duty cycles can be expressed as follows:

$$D_{buck} = \frac{V_{out}}{V_{in\_max}\eta_{buck}} \tag{23}$$

$$D_{boost} = 1 - \frac{V_{in\_min}\eta_{boost}}{V_{out}} \tag{24}$$

where D_{buck} is the duty cycle of the buck mode (%), D_{boost} is the duty cycle of the boost mode (%), V_{in_min}, V_{in_max}, and V_{out} are the minimum, maximum input voltage, and output voltage (V) of the converter, respectively. η_{buck} and η_{boost} are the efficiencies of the converter which are estimated to equal 90% for buck mode and 80% for boost mode, respectively.

3. Energy Management Control Strategy

In this work, the proposed control strategy is designed to determine the power distribution of three electrical sources based on the load power demand and SOC of ESS. Additionally, the control scheme of the DC bus voltage regulation is considered to guarantee stable voltage during power fluctuation and track the speed limitation of the power converter. The block diagram of the proposed control strategy is described in Figure 8.

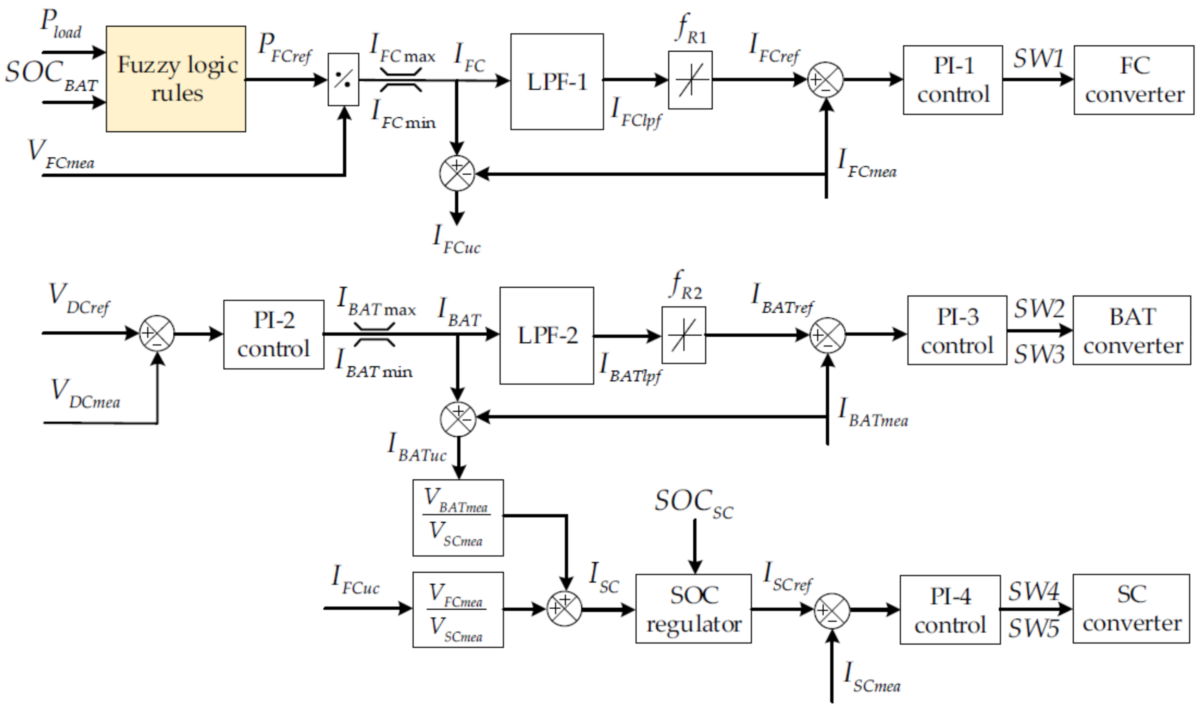

Figure 8. Energy control strategy for the HPS.

3.1. Control Strategy Description

In this hybrid system, the PEMFC is utilized as a primary source that not only supplies power for the traction load, but also ensures the SOC level of the BAT within the desired range. As a result, the load power demand (P_{load}) and the SOC_{BAT} are taken as two inputs for the FLRs [37] to generate the reference PEMFC power (P_{FCref}). This power is divided by the measurement value of the PEMFC voltage to create the PEMFC current (I_{FC}). This current is passed to the low-pass filter (LPF-1) to decompose into low- and high-frequency currents, and given as the reference current (I_{FCref}) and uncompensated current (I_{FCuc}) of the PEMFC. For the BAT, it is used to keep the DC bus voltage at the reference value through the voltage control loop. The reference (V_{DCref}) and measured (V_{DCmea}) DC bus voltage are compared with each other, and the difference voltage then is provided to the PI controller (PI-2 control) to produce the DC bus current (I_{BAT}). This current is decomposed by using the low-pass filter (LPF-2) into low- and high-frequency currents, which are then used as the BAT's reference current (I_{BATref}) and uncompensated current (I_{BATuc}). Due to the fast dynamic response, the SC will take care of the uncompensated current of the PEMFC and BAT. Thus, the SC reference current (I_{SCref}) consists of a high-frequency component and an error component of the PEMFC current and BAT current.

In this strategy, the FLRs are inherited from our previous papers in [15,37] to calculate the reference power of the PEMFC based on the load power demand and SOC level of BAT. These rules have two input variables (P_{load}, SOC_{BAT}) and one output variable (P_{FCref}). Seven membership functions (MFs) are used to characterize the input variable P_{load} including NH (Negative High), NM (Negative Medium), NL (Negative Low), Z (Zero), PL (Positive Low), PM (Positive Medium), and PH (Positive High) within the range of (−1,1). For the input variable SOC_{BAT}, five MFs divided into VL (Very Low), L (Low), M (Medium), H (high), and VH (Very High) with the scope as (0.4, 0.9). The output P_{FCref} is characterized by five MFs: Min (Minimum), ML (Medium-Low), M (Medium), MH (Medium-High), and Max (Maximum). The inhomogeneous MFs of the inputs and output are depicted in Figure 9 and the fuzzy rules are described in Table 4.

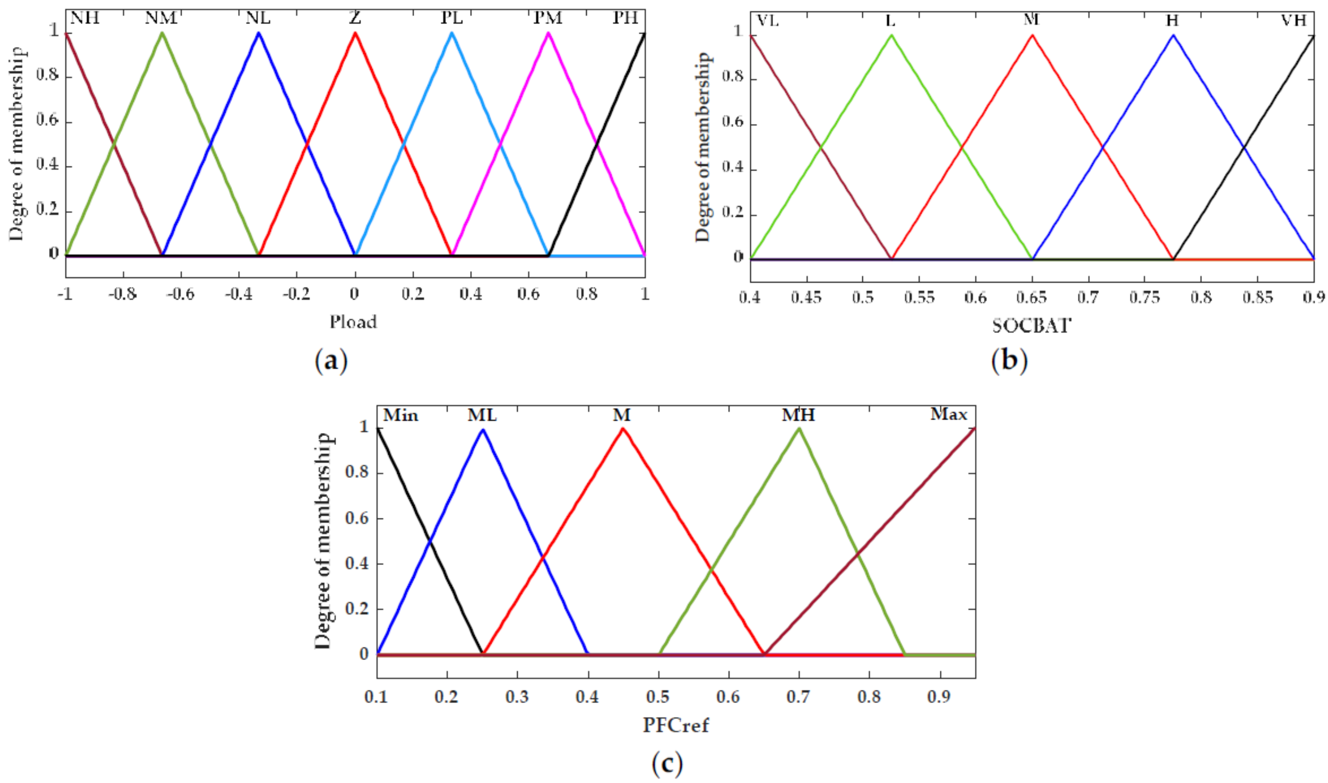

Figure 9. Inputs and output membership functions of the FLRs [15,37]. (**a**) Input variable P_{load}; (**b**) Input variable SOC_{BAT}; (**c**) Output variable P_{FCref}.

Table 4. Fuzzy rules for the inputs and output membership functions [15].

P_{FCref}		P_{load}						
		NH	**NM**	**NL**	**Z**	**PL**	**PM**	**PH**
SOC_{BAT}	VL	Min	Min	ML	M	M	MH	Max
	L	Min	Min	Min	ML	ML	M	MH
	M	Min	Min	Min	Min	ML	M	MH
	H	Min	Min	Min	Min	Min	M	MH
	VH	Min	Min	Min	Min	Min	ML	M

The suggested fuzzy rules distribute the needed power to the PEMFC source in order to not only supply the workload requirement, but also maintain the SOC supplement of the BAT. For instance, during the charging process, if the SOC of BAT is at a high level, the injected power is lower, and vice versa. Meanwhile, during the discharging process, if the SOC of BAT is at a high level, the BAT will release more output power and vice versa.

Furthermore, low-pass filters are applied to decompose the demand current that corresponds to the operating ranges and power changing rate of the PEMFC, BAT, and SC, using the Ragone diagram theory [35] and the dynamic features of energy sources. This approach is advantageous for experimental applications because of its rapid computation time and simple design. For the PEMFC, the low-frequency current is derived from the required PEMFC current as follows:

$$I_{FClpf} = f_{LPF-1}(I_{FC}) \tag{25}$$

where I_{FClpf} is the PEMFC low-frequency current (A), I_{FC} is the required PEMFC current (A), $f_{LPF-1}(.)$ is the function of the low pass filter (LPF-1).

To achieve the PEMFC reference current, a rate limiter is employed to limit the discharge rates of the PEMFC current as given.

$$I_{FCref} = f_{R1}(I_{FClpf}) \tag{26}$$

where I_{FCref} is the PEMFC reference current (A), and $f_{R1}(.)$ is the function of the rate limiter for the PEMFC current.

This reference current and measured PEMFC current are compared with each other, and the different current is supplied to the PI-1 controller to generate the control signal (*SW1*) for the PEMFC converter. In addition, the uncompensated PEMFC current is given by

$$I_{FCuc} = I_{FC} - I_{FCmea} \tag{27}$$

where I_{FCuc} is the uncompensated PEMFC current (A), and I_{FCmea} is the measured PEMFC current (A).

Similarly, for the BAT, the reference and uncompensated currents can be defined by using the low-pass filter and a rate limiter as follows [43]:

$$I_{BATlpf} = f_{LPF-2}(I_{BAT}) \tag{28}$$

$$I_{BATref} = f_{R2}(I_{BATlpf}) \tag{29}$$

$$I_{BATuc} = I_{BAT} - I_{BATmea} \tag{30}$$

where I_{BATlpf} is the BAT low-frequency current (A), I_{BAT} is the required BAT current (A), $f_{LPF-2}(.)$ is the function of the low pass filter (LPF-2), $f_{R2}(.)$ is the function of the rate limiter for the BAT current, and I_{BATref}, I_{BATuc}, and I_{BATmea} are the reference, uncompensated, and measured current of the BAT, respectively (A).

From the above equations, the required BAT current (I_{BAT}) is the output of the DC bus voltage control. In the hybrid power system, this control plays an important role to guarantee the system's stability because if the load power demand rises suddenly, the DC bus voltage drops, and vice versa. In order to control the output voltage of the DC bus, a PI-2 controller is designed, as shown in Figure 8. Herein, this controller will generate the current I_{BAT} based on the deviation between the measured DC output voltage (V_{DCmea}) and a reference (V_{DCref}) as the input signal.

Due to the slow dynamics, the PEMFC and BAT cannot instantly adapt to high-frequency currents. Additionally, due to the presence of electrical inertia in DC/DC converters, the PEMFC converter and BAT converter may not quickly track the reference currents. Thus, the SC, with the high power density and fast dynamics response, is employed to compensate for the high-frequency component and the error due to the slow dynamics of the PEMFC and BAT currents. The required SC current is given by

$$
\begin{aligned}
I_{SC} &= I_{FCuc} \cdot \frac{V_{FCmea}}{V_{SCmea}} + I_{BATuc} \cdot \frac{V_{BATmea}}{V_{SCmea}} \\
&= \left(I_{FC} - I_{FCmea} + I_{FCref} - I_{FCref} \right) \cdot \frac{V_{FCmea}}{V_{SCmea}} + \left(I_{BAT} - I_{BATmea} + I_{BATref} - I_{BATref} \right) \cdot \frac{V_{BATmea}}{V_{SCmea}} \\
&= \left(\left(I_{FC} - I_{FCref} \right) + \left(I_{FCref} - I_{FCmea} \right) \right) \cdot \frac{V_{FCmea}}{V_{SCmea}} + \left(\left(I_{BAT} - I_{BATref} \right) + \left(I_{BATref} - I_{BATmea} \right) \right) \cdot \frac{V_{BATmea}}{V_{SCmea}} \\
&= \left(I_{FChf} - I_{FCerr} \right) \cdot \frac{V_{FCmea}}{V_{SCmea}} + \left(I_{BAThf} - I_{BATerr} \right) \cdot \frac{V_{BATmea}}{V_{SCmea}}
\end{aligned}
\tag{31}
$$

where $I_{FChf}\left(= I_{FC} - I_{FCref}\right)$ and $I_{BAThf}\left(= I_{BAT} - I_{BATref}\right)$ are the high-frequency current of I_{FC} and I_{BAT} (A), respectively; $I_{FCerr}\left(= I_{FCref} - I_{FCmea}\right)$ and $I_{BATerr}\left(= I_{BATref} - I_{BATmea}\right)$ are the error of the PEMFC and BAT currents due to the slow dynamic of each source (A), respectively. Then, the SC references current is given as the output of the SOC regulator that guarantees the SOC of SC in the limited ranges as follows [37]:

$$
I_{SCref} = \begin{cases} \alpha |I_{SC}| & if \quad SOC_{SC} \leq SOC_{SC\min} \\ I_{SC} & if \quad SOC_{SC\min} < SOC_{SC} < SOC_{SC\max} \\ \beta |I_{SC}| & if \quad SOC_{SC} \geq SOC_{SC\max} \end{cases}
\tag{32}
$$

where I_{SCref} is the reference current of the SC (A), I_{SC} is the required SC current (A), SOC_{SC} is the SOC level of the SC, $SOC_{SC\min}$ and $SOC_{SC\max}$ are the minimum and maximum allowable of the SOC_{SC}, respectively, and α and β are the tuning parameters, as referred to in [37].

3.2. PI Controller Design for the HPS

In this work, four PI controllers are designed to generate the duty cycle for the PWM generator of DC/DC converters and regulate the DC bus voltage. The current control loop of the PEMFC boost converter is controlled by the PI-1 controller. The PI-2 controller is the outer voltage control loop to maintain the DC bus voltage, while the PI-3 controller is the inner current control loop for the BAT's bidirectional buck–boost converter. Meanwhile, the PI-4 controller is designed for use in the current control loop of the SC's bidirectional buck–boost converter. In the bidirectional converter, because both buck (charge direction) and boost (discharge direction) modes employ a similar transfer function of the control loops, the operating characteristics of the boost mode are taken into account while designing the controller.

In the control parameters' design process, the controller gains of the SC converter are designed first because the SC has a faster dynamic response than the BAT and PEMFC. In addition, the current control loop bandwidth (BW) of the PI-4 controller is selected as higher than the BW of other controllers. Similarly, the current control loop BW of the PI-3 controller is chosen as lesser than the PI-4 controller, but higher than the PI-1 controller because the BAT charge/discharge rates are slower than the SC, but faster than the PEMFC. Moreover, the BW of the BAT and PEMFC current controller is designed such that high-frequency components are transferred to the SC for power or current compensation. In this work, the current control loop BW of the PI-4, PI-3, and PI-1 controllers is limited to equal 1/6, 1/10, and 1/14 of the switching frequency (f_{sw}) of the DC/DC converter, respectively [43]. Furthermore, to regulate the DC bus voltage, the voltage control loop BW is chosen to be smaller than the current control loop of the BAT because the current control loop has a faster response than the voltage control loop.

3.2.1. Design of SC Current Controller (PI-4 Controller)

In the control strategy, SC is used as the ESS to compensate for the response of BAT and PEMFC. The controller of the SC converter is designed by using the reference and measured SC current. Thus, the characteristics of the current control loop are considered to guarantee the stability of the current controller. The block diagram of the SC current control loop is presented in Figure 10. The duty-cycle-to-current transfer function of the SC converter is given by [44].

$$G_{id\_SC}(s) = \frac{2V_o}{(1-D_{SC})^2 R} \frac{\left(1+\frac{RC_2}{2}s\right)}{1+\frac{L}{(1-D_{SC})^2 R}s+\frac{LC_2}{(1-D_{SC})^2}s^2} \tag{33}$$

where V_o is the output voltage of the converter (V) and D_{SC} is the duty cycle of the SC converter (%).

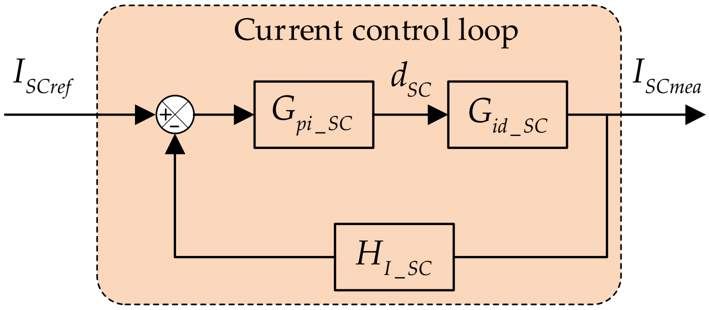

Figure 10. Current controller diagram of the SC converter.

To achieve the desired crossover frequency and stability margin of the transfer function (33), the PI compensator (PI-4 controller) is designed as follows:

$$G_{pi\_SC}(s) = K_{p\_SC} + K_{i\_SC}\frac{1}{s} \tag{34}$$

where K_{p_SC} and K_{i_SC} are the PI compensator gains.

The transfer function of the compensated current control loop of the SC converter is defined as

$$T_{i\_SC}(s) = G_{pi\_SC}(s) \cdot G_{id\_SC}(s) \cdot H_{I\_SC} \tag{35}$$

where H_{I_SC} is the current sensor gain.

The parameters of electronic components used in the SC converter are given in Table 5. The Bode diagram of the SC current control loop with and without using the PI compensator is shown in Figure 11. As a result of using the PI compensator, the phase margin (PM) decreases from 90° to 60.1° at 2.09×10^4 rad/s, ensuring the stability of the current control loop for the SC converter. The PI-4 controller parameters are $K_{p\_SC} = 0.0257$ and $K_{i\_SC} = 307.3101$.

Table 5. Parameters of the SC converter.

Parameter	Value	Parameter	Value
V_o	48 (V)	C_2	2590 (uF)
V_{in_SC}	24 (V)	D_{SC}	0.5
H_{I_SC}	1	L	68 (uH)
R	50 (mΩ)	f_{sw}	20 (kHz)

3.2.2. Design of BAT Current Controller (PI-3 Controller)

In the control strategy, the BAT is used to guarantee the DC bus voltage. Thus, two control loops are applied in which the inner loop is the current control and the outer loop is the voltage control. The block diagram of the BAT controllers is shown in Figure 12. The voltage control loop produces the reference current to the BAT (I_{BATref}) that is then compared to the measured BAT current to generate the input signal in the current control loop. The transfer function of duty-cycle-to-current is described as follows [44].

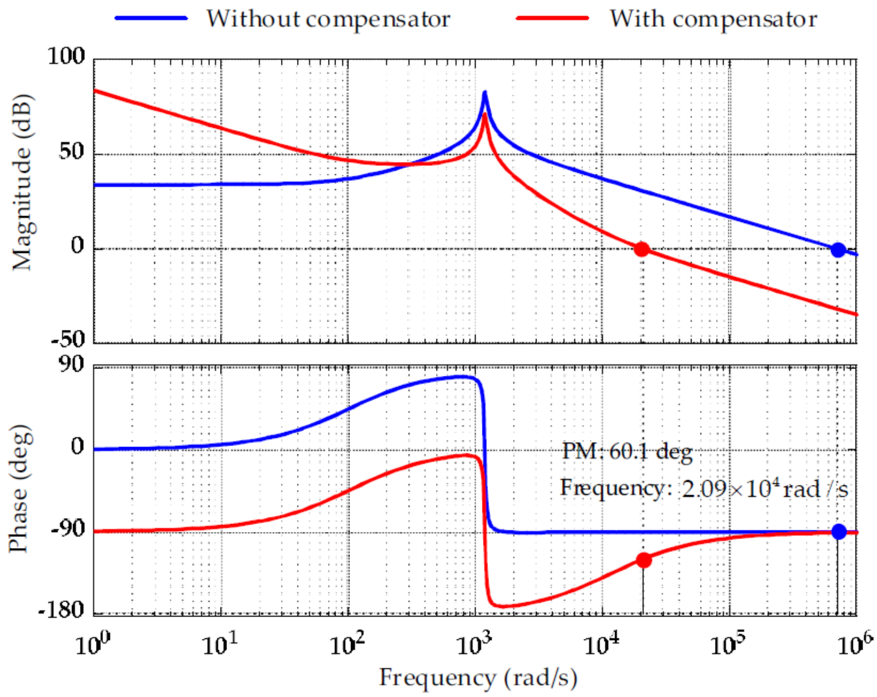

Figure 11. Bode diagram of the SC current control loop.

$$G_{id\_BAT}(s) = \frac{2V_o}{(1-D_{BAT})^2 R} \frac{\left(1+\frac{RC_2}{2}s\right)}{1+\frac{L}{(1-D_{BAT})^2 R}s+\frac{LC_2}{(1-D_{BAT})^2}s^2} \quad (36)$$

where V_o is the output voltage of the converter (V) and D_{BAT} is the duty cycle of the BAT converter (%).

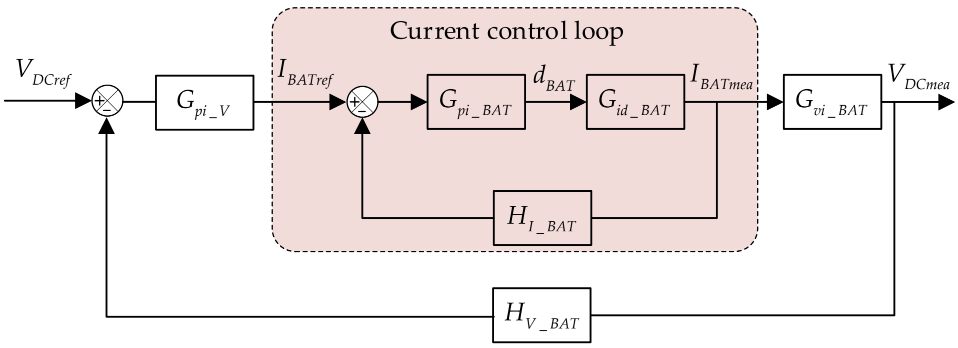

Figure 12. Block diagram of the controllers for BAT converter.

The PI compensator of the BAT current control loop (PI-3 controller) is given as

$$G_{pi\_BAT}(s) = K_{p\_BAT} + K_{i\_BAT}\frac{1}{s} \quad (37)$$

where K_{p_BAT} and K_{i_BAT} are the gains of the PI controller.

The transfer function of the current control loop is described as

$$T_{i\_BAT}(s) = G_{pi\_BAT}(s) \cdot G_{id\_BAT}(s) \cdot H_{I\_BAT} \quad (38)$$

where H_{I_BAT} is the current sensor gain.

The parameters of the BAT converter are given in Table 6. The Bode plot of the BAT current control loop with and without the PI compensator is shown in Figure 13. The PM with the PI compensator is 60°, which achieves the stability of the current control loop at 1.26×10^4 rad/s. The PI-3 controller parameters are $K_{p\_BAT} = 0.0153$ and $K_{i\_BAT} = 110.1810$.

Table 6. Parameters of the BAT converter.

Parameter	Value	Parameter	Value
V_o	48 (V)	C_2	2590 (uF)
V_{in}	21.6 (V)	D_{BAT}	0.55
H_{I_FC}	1	L	68 (uH)
R	50 (mΩ)	f_{sw}	20 (kHz)

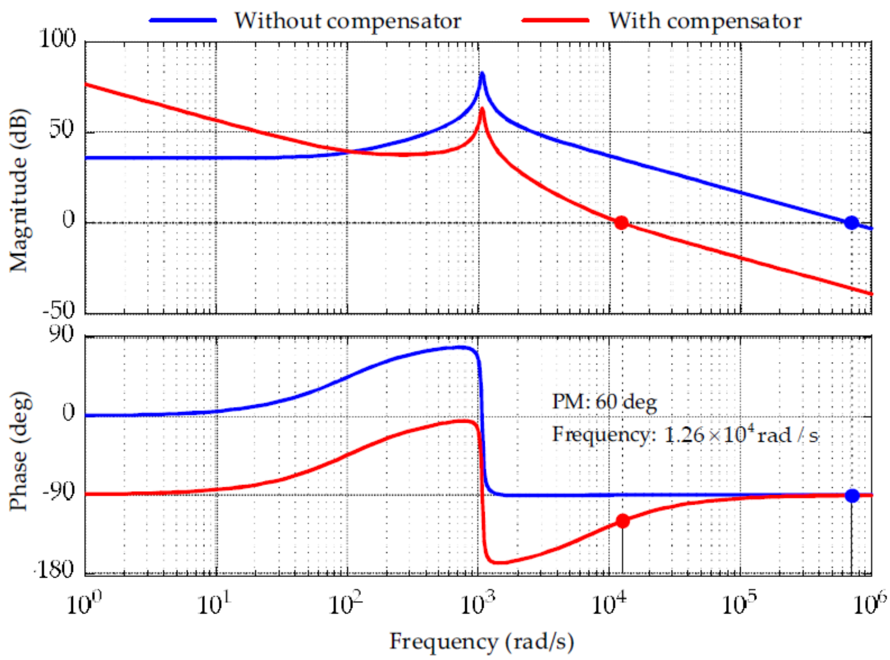

Figure 13. Bode diagram of the BAT current control loop.

3.2.3. Design of DC Bus Voltage Controller (PI-2 Controller)

In this work, the BAT is employed to keep the DC bus voltage at the desired value. As a result, the DC bus voltage controller is based on the outer voltage control loop of the BAT converter. The transfer function of the voltage control loop is given as [44].

$$G_{vi\_BAT}(s) = \frac{R(1 - D_{BAT})\left(1 - \frac{L}{R(1-D_{BAT})^2}s\right)}{2 + RC_2 s} \tag{39}$$

Due to the slower response than the inner current control loop, the outer voltage control loop has a lesser bandwidth than the current control loop. The PI compensator transfer function of the voltage control loop (PI-2 controller) is given as

$$G_{pi\_V}(s) = K_{p\_V} + K_{i\_V}\frac{1}{s} \tag{40}$$

where K_{p_V} and K_{i_V} are the gains of the PI-2 controller.

The transfer function of the voltage control loop is described as

$$T_v(s) = G_{pi\_V}(s) \cdot G_{vi\_BAT}(s) \cdot H_{V\_BAT} \tag{41}$$

where H_{V_BAT} is the voltage sensor gain.

The Bode plot of the voltage control loop with and without the PI compensator is shown in Figure 14. The DC bus voltage controller is designed such that the PM of 59.4° is at 1.26×10^4 rad/s. The PI-2 controller parameters are $K_{p\_V} = 6.1436$ and $K_{i\_V} = 482.52$.

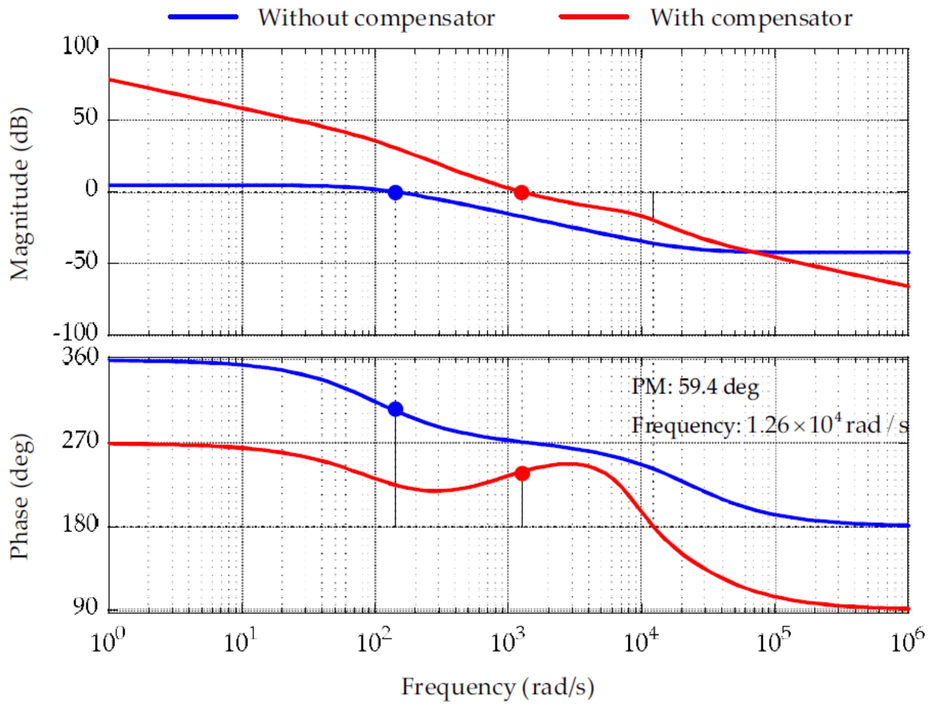

Figure 14. Bode diagram of the DC bus voltage control loop.

3.2.4. Design of PEMFC Current Controller (PI-1 Controller)

In this hybrid system, the PEMFC is used as the primary source to supply the power for the load power demand. The block diagram of the current controller for the PEMFC is presented in Figure 15. The duty-cycle-to-current transfer function of the PEMFC converter is given by [44].

$$G_{id\_FC}(s) = \frac{2V_o}{(1 - D_{FC})^2 R} \frac{\left(1 + \frac{RC_2}{2} s\right)}{1 + \frac{L}{(1-D_{FC})^2 R} s + \frac{LC_2}{(1-D_{FC})^2} s^2} \tag{42}$$

where V_o is the output voltage of the converter (V) and D_{FC} is the duty cycle of the FC converter (%).

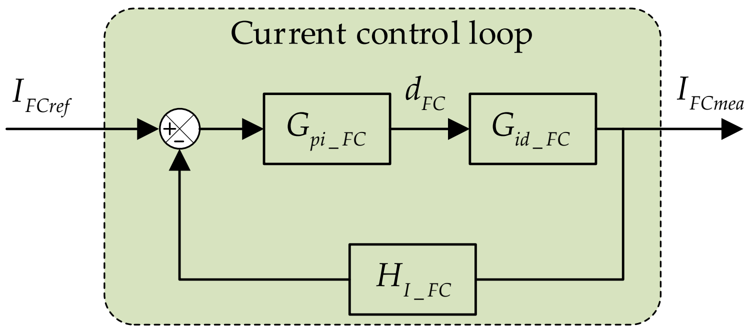

Figure 15. Current controller diagram of the PEMFC converter.

The PI compensator (PI-1 controller) is designed as follows:

$$G_{pi\_FC}(s) = K_{p\_FC} + K_{i\_FC} \frac{1}{s} \tag{43}$$

where K_{p_FC} and K_{i_FC} are the PI compensator gains.

The compensated current control loop of the PEMFC converter is given by

$$T_{i\_FC}(s) = G_{pi\_FC}(s) \cdot G_{id\_FC}(s) \cdot H_{I\_FC} \tag{44}$$

where H_{I_FC} is the current sensor gain.

The parameters of the PEMFC converter are given in Table 7. The Bode diagram of the SC current control loop with and without using the PI compensator is shown in Figure 16. The result of PM with a PI compensator is 60° at 8.98×10^3 rad/s, which can achieve the stability of the current control loop for the PEMFC converter. The PI-1 controller parameters are $K_{p\_FC} = 0.0104$ and $K_{i\_FC} = 23.3103$.

Table 7. Parameters of the PEMFC converter.

Parameter	Value	Parameter	Value
V_o	48 (V)	C_2	2590 (uF)
V_{in_FC}	24 (V)	D_{FC}	0.5
H_{I_FC}	1	L	68 (uH)
R	50 (mΩ)	f_{sw}	20 (kHz)

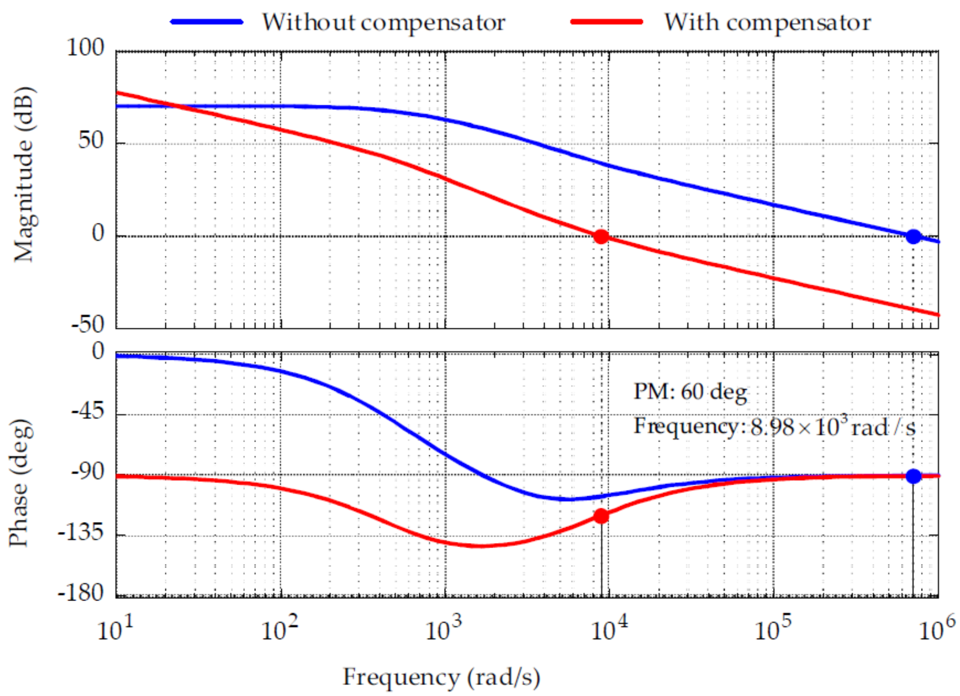

Figure 16. Bode diagram of the PEMFC current control loop.

4. Simulation Results

In this section, simulation results are conducted with several levels of the load power profile in the form of power steps, such as acceleration and deceleration in practical applications. The proposed control strategy is compared with the other two strategies [37] consisting of RB-EMS and F-EMS to demonstrate the performance during the fluctuation of the load power demand. In addition, the modeling of the HPS is carried out in a MATLAB/Simulink environment, with a sampling time of 0.05 ms set up for displaying simulation results. The simulation model of the proposed EMS is presented in Figure 17. Specifications of energy sources and parameters of the proposed EMS are given in Tables 8–11.

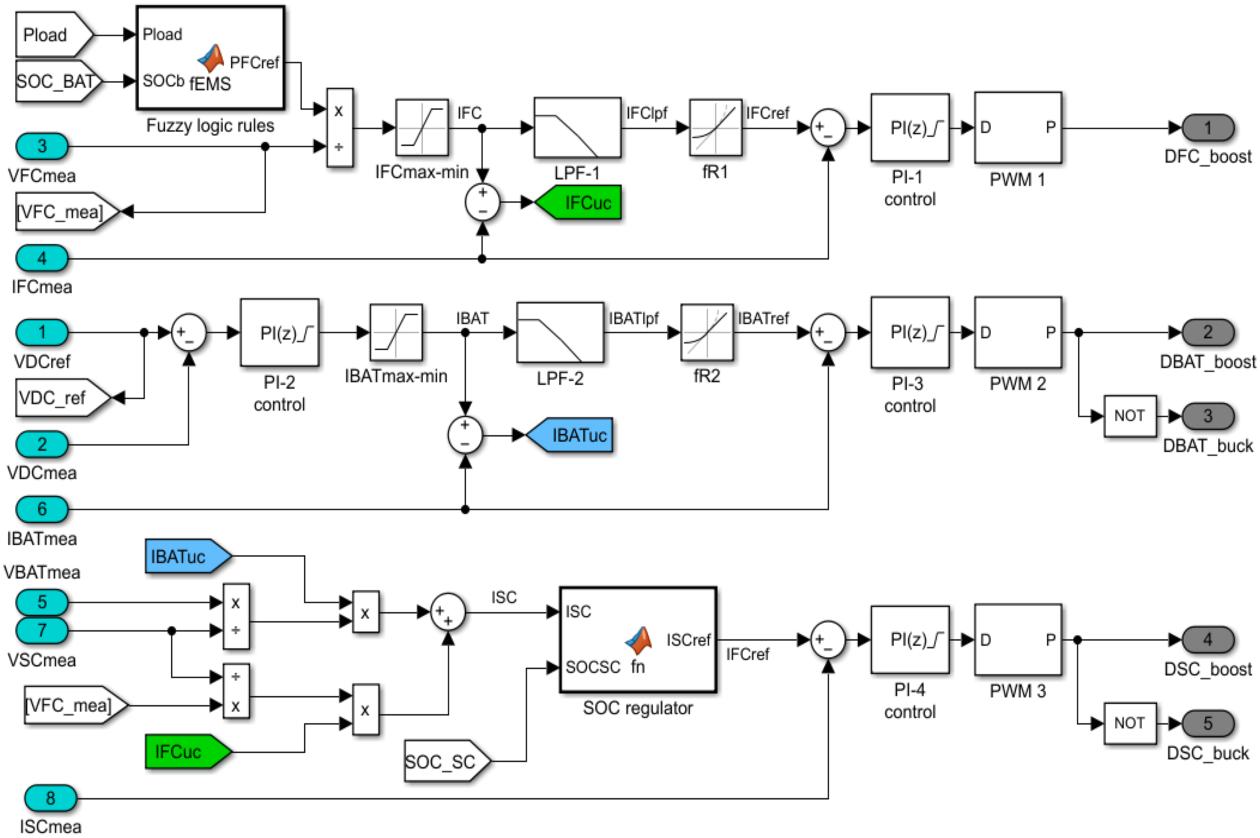

Figure 17. The simulation model of the proposed EMS.

Table 8. PEMFC specifications.

Parameter	Value
Nominal operation point (U_{nom}, I_{nom})	(24 V, 8.3 A)
Maximum operating point (U_{max}, I_{max})	(20 V, 12 A)
Number of cells	40
Nominal power	200 W
Nominal efficiency	40%
Nominal hydrogen pressure	0.45–0.55 bar
Nominal air pressure	2 bar
Nominal air flow rate	2.6 lpm
Maximum stack temperature	65 °C
Cooling	Air

Table 9. SC bank parameters.

Parameter	Value
Number of series capacitor bank	9
Rated voltage	24 V
Capacitance	50 F
Operating temperature	25 °C

Table 10. BAT parameters.

Parameter	Value
Rated capacity	12.8 Ah
Nominal voltage	21.6 V
Number of cells	6

Table 11. Proposed control strategy parameters.

Parameter	Value	Parameter	Value
SOC_{BAT_min}	0.6	η_P	0.007
SOC_{BAT_max}	0.9	η_I	0.05
f_{LPF-1}	10 Hz	f_{LPF-2}	32 Hz
V_{DCref}	48 (V)		

The hybrid system performance and control strategy effectiveness are described in Figures 18–22. First of all, Figure 18 depicts the adaptation of the load power using three EMSs, with a continuous black line representing the reference power of the load, a dashed-dot blue line indicating the power of the RB-EMS, a dashed-dot green line showing the power of the F-EMS, and a continuous red line displaying the output power of the proposed-EMS. As shown in Figure 18a, when the load power is abruptly changed at the time of the 5th, 10th, 15th, 20th, 25th, 30th, 40th, 45th, 50th, 55th, 60th, and 65th second, the released power of the proposed-EMS meets the load requirements better than the RB-EMS and F-EMS under operating circumstances. At the moment of transient peak power, although the PEMFC cannot instantaneously respond to load changes owing to the lowest dynamics, the load tracking effort may still be assured due to compensation from the BAT and SC. In addition, the power tracking error of three EMSs was presented in Figure 18b. The proposed EMS gets the optimum distributed accuracy with the error of $(-2.1 \rightarrow 2.6)$ W, while the F-EMS has an inadequate power approximated $(-8.2 \rightarrow 4.4)$ W, and the RB-EMS takes the inaccuracy power up to $(-11 \rightarrow 19)$ W. Consequently, the proposed EMS has the lowest average insufficient power on the hybrid system's load profile. This demonstrates that the proposed approach can absolutely assure the load power demand during different operational situations.

Next, based on the positive results of the proposed EMS, the power distributions of the PEMFC, BAT, and SC in the hybrid system are shown in Figure 19. Due to a primary power source, the PEMFC supplies the majority of the load power demand and has a power distribution higher than the BAT and SC. However, the released power of PEMFC cannot satisfy the required load power in the transient state. As a result, BAT offers uncompensated power that supports the PEMFC in a steady state to lessen the power fluctuation of the PEMFC. Conversely, the SC bank decreases the fluctuating power of the PEMFC and BAT by supplying the peak power that the PEMFC cannot provide in the transient state when the load changes quickly. The power compensation from the BAT and SC maintains the load tracking performance at each moment of transient peak power, even if the PEMFC, with the lowest dynamics, cannot react to the change in load right away.

The comparison of the DC bus voltage using three EMSs is depicted in Figure 20. The proposed EMS maintains the DC bus voltage stably at around 48 V with less fluctuation than the RB-EMS and F-EMS. In particular, the proposed EMS produces a DC bus peak voltage in the range of $(47.8 \rightarrow 48.3)$ V, which is approximated by a 1% voltage ripple during the step-change interval of the load. Meanwhile, the fluctuation of the DC bus voltage under F-EMS has peak values within $(46.8 \rightarrow 48.9)$ V by a 4.375% ripple. This result is better than the ones using the RB-EMS with the peak voltage in the range of $(46.5 \rightarrow 49.5)$ V by 6.25% ripple.

Figure 21 depicts the simulation results for both BAT and SC SOC, which characterize the charge and discharge state at each timeline when the load changes. As shown in Figure 21a, the proposed EMS can hold the SOC BAT level better than the RB-EMS and F-EMS in the first 20 s of low load power demand. However, the proposed EMS shows faster SOC degradation than RB-EMS and F-EMS after 20 s under high load power consumption. In contrast, for the SC, the proposed EMS achieves a SOC varying range within $(83.85 \rightarrow 84.05)$ % which is stable and lower than the RB-EMS with the range of $(82.15 \rightarrow 84.05)$ %, while F-EMS has a large fluctuation in $(81.85 \rightarrow 84.05)$ %, as presented in Figure 21b.

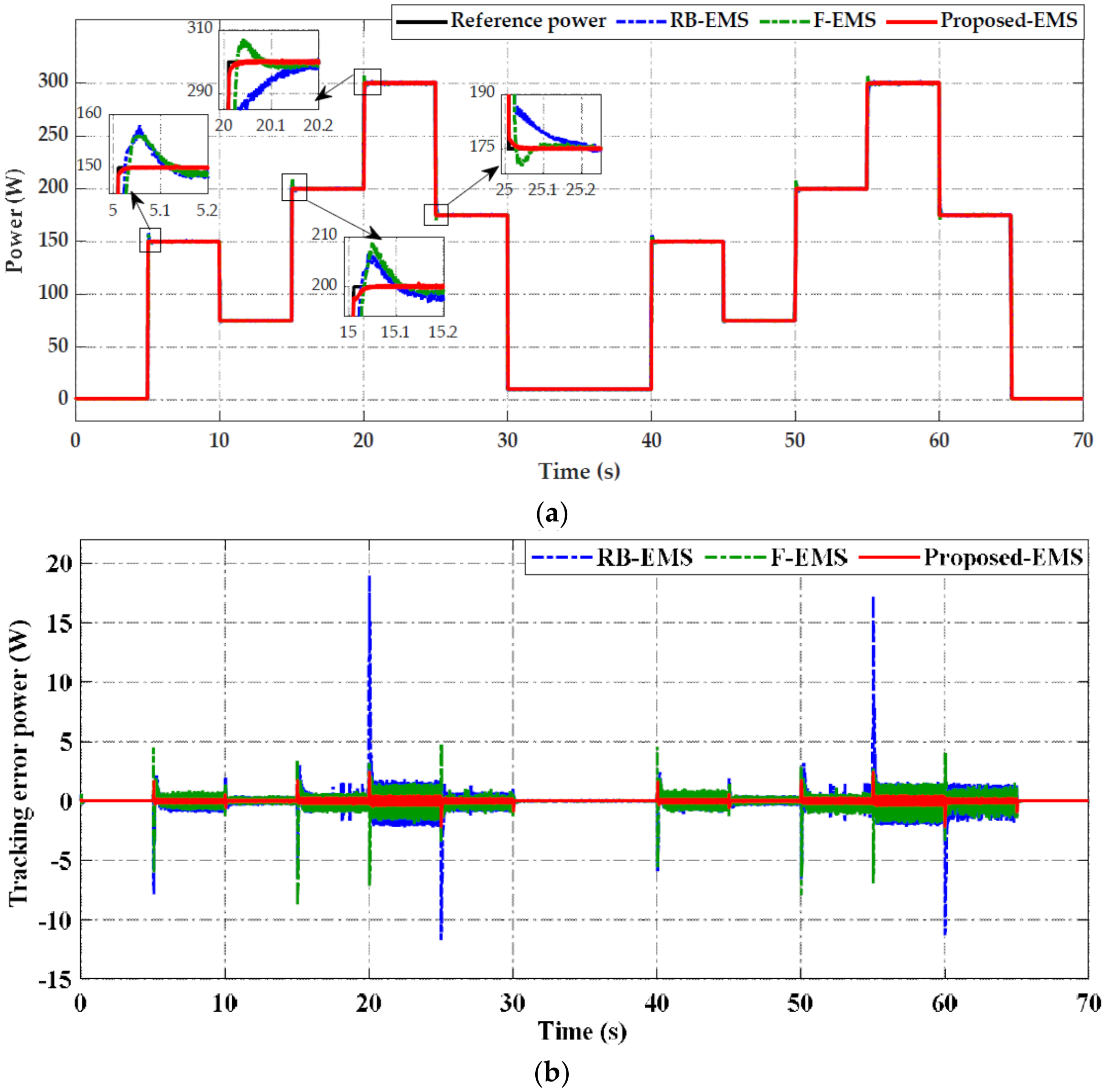

Figure 18. The comparison power of three EMSs. (**a**) The adaptation of load power. (**b**) The tracking error power.

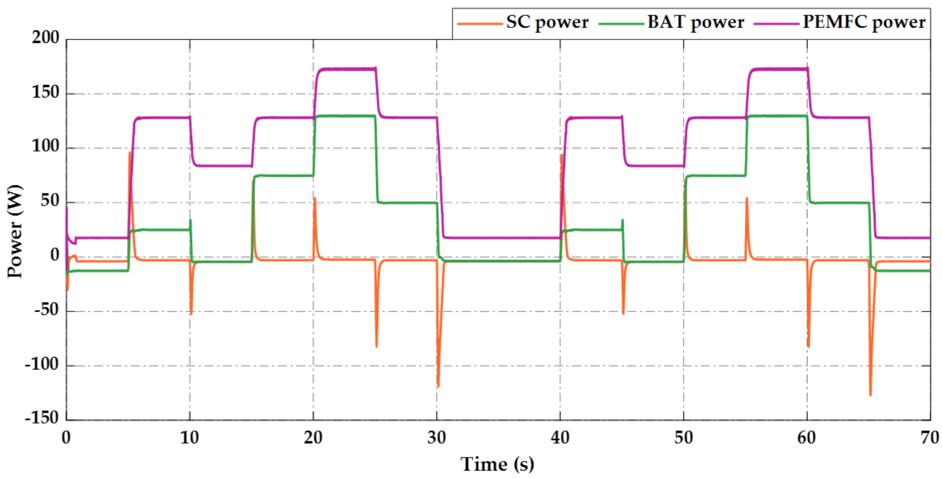

Figure 19. The power distribution from energy sources.

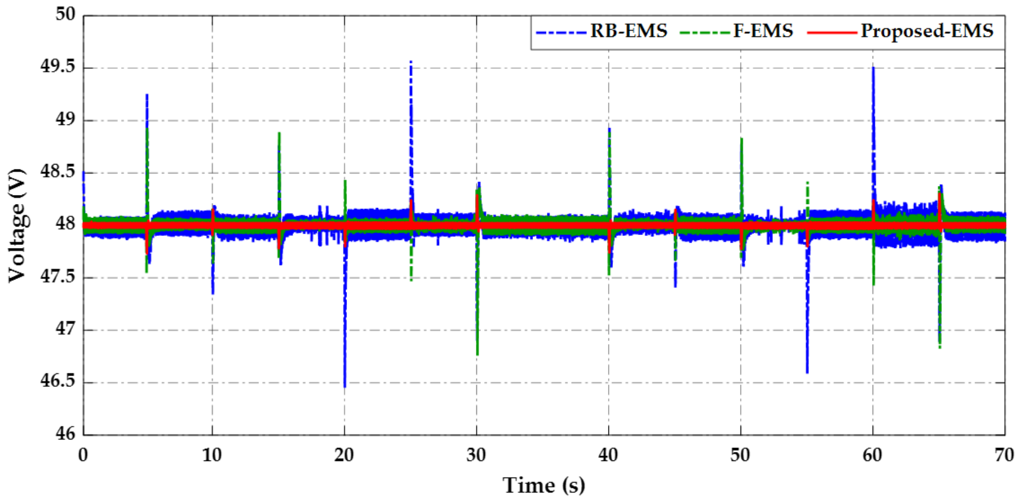

Figure 20. The comparison of the DC bus voltage.

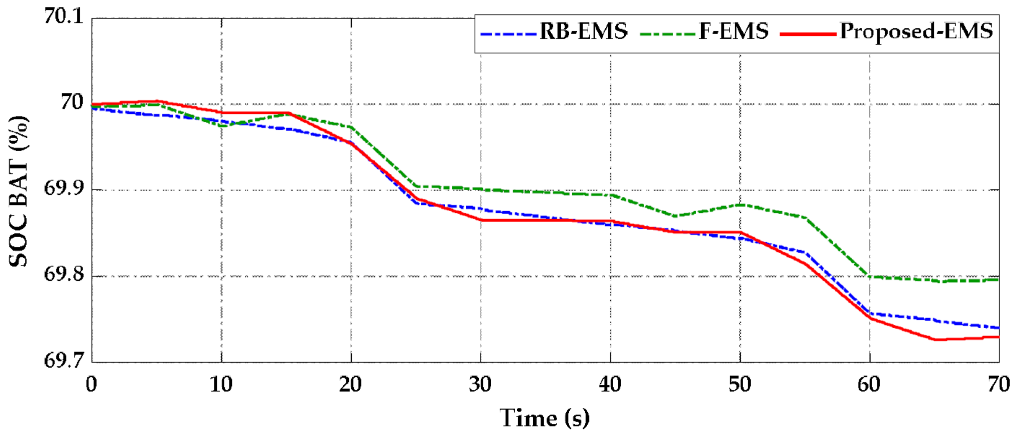

(**a**)

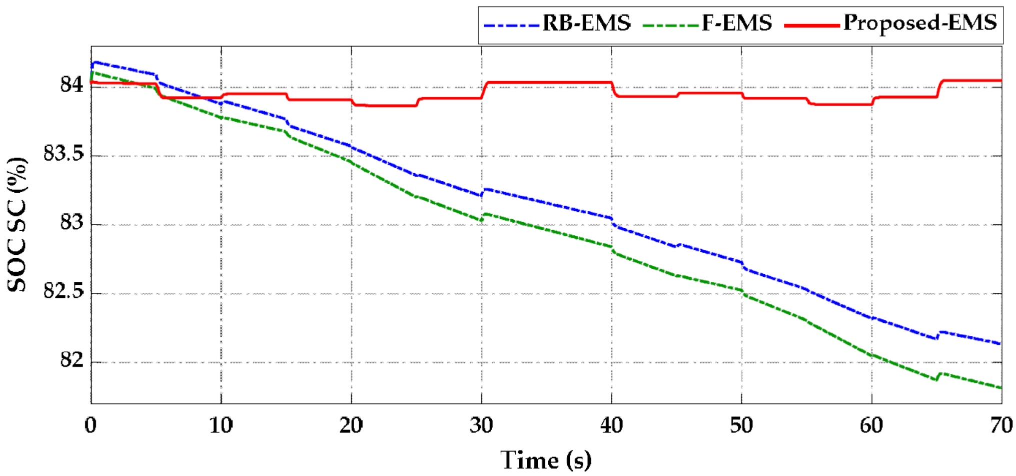

(**b**)

Figure 21. The SOC comparison. (**a**) BAT. (**b**) SC.

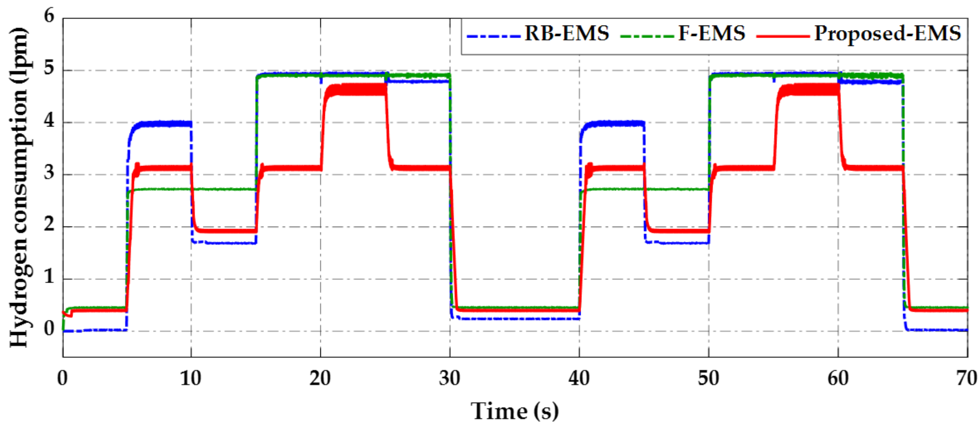

Figure 22. The comparison of hydrogen consumption of PEMFC stack.

Finally, Figure 22 illustrates the hydrogen consumption of three EMSs. As a result, the proposed-EMS consumes less hydrogen fuel than the RB-EMS and F-EMS based on the amount of fuel consumption. The highest fuel economy of the RB-EMS and F-EMS in comparable operating conditions is 5 lpm, however, in the case of the proposed approach, hydrogen consumption is 4.8 lpm at the time of a maximum load power demand. With hydrogen consuming less than 0.2 lpm compared to other ways, it demonstrates that the proposed strategy delivers superior fuel efficiency.

5. Conclusions

This study proposed a new hierarchical approach-based EMS considering the DC bus voltage regulation to correctly distribute energy from the load power demand to the PEMFC, BAT, and SC, while also maintaining DC bus voltage stability. In detail, the FLRs and LPFs were used to determine the reference currents of power sources based on their dynamic response. In addition, the controller design approach for DC/DC converters was proposed based on the dynamic characteristics and response of converters to guarantee the system performance and maintain the stability of the DC bus voltage. Simulation results showed that the proposed technique achieved the highest accuracy in distributed power with an error of $(-2.1 \rightarrow 2.6)$ W to satisfy the load power demand, maintain the stability of the DC bus voltage with the least voltage ripple of approximately 1%, and increase the efficiency of the PEMFC system during the step-change interval of the load in comparison to the other strategies. The issues of achieving optimum fuel economy and enhancing PEMFC efficiency, however, were not thoroughly covered in this study and need to be further investigated. In addition, the advanced configuration of the DC-DC converters and improved controllers should be considered to reduce the voltage ripple of the DC bus, which can increase the system performance, quickly adapt to the high peak power, and extend the lifetime of energy devices. As a result, this work served as a foundation for the future development of sophisticated EMSs for hybrid PEMFC applications.

Author Contributions: K.K.A. was the supervisor providing funding and administrating the project, and he reviewed and edited the manuscript. H.-A.T. carried out the investigation, and methodology, built and validated the hybrid model through MATLAB simulation, and wrote the original manuscript. V.-D.P. validated the proposed control strategy and analyzed the methodology by using MATLAB simulation. H.-V.-A.T. supported the model and methodology in MATLAB simulations and checked the manuscript. All authors have read and agreed to the published version of the manuscript.

Funding: This research was financially supported by the "Hydrogen Electric Tram Demonstration Project" through the Ministry of Trade, Industry, and Energy (MOTIE) and the Korea Institute for Advancement of Technology (KIAT) (G02P16110000511), and this work was supported by "Regional Innovation Strategy (RIS)" through the National Research Foundation of Korea (NRF) funded by the Ministry of Education (MOE) (2021RIS-003).

Institutional Review Board Statement: Not applicable.

Informed Consent Statement: Not applicable.

Data Availability Statement: The load profile data presented in this study are available in [37] (accessed on 20 July 2022).

Conflicts of Interest: The authors declare no conflict of interest.

References

1. Li, Z.; Khajepour, A.; Song, J. A comprehensive review of the key technologies for pure electric vehicles. *Energy* **2019**, *182*, 824–839. [CrossRef]
2. Trinh, H.-A.; Truong, H.V.A.; Do, T.C.; Nguyen, M.H.; Phan, V.D.; Ahn, K.K. Optimization-based energy management strategies for hybrid construction machinery: A review. *Energy Rep.* **2022**, *8*, 6035–6057. [CrossRef]
3. MacEwen, R. *The Hidden Problems Within the Electric Vehicle Battery Supply Chain*; Ballard Power Systems Inc.: Vancouver, BC, Canada, 2019; Available online: https://blog.ballard.com/electric-vehicle-battery-supply-chain (accessed on 20 July 2022).
4. Li, Q.; Chen, W.; Liu, Z.; Li, M.; Ma, L. Development of energy management system based on a power sharing strategy for a fuel cell-battery-supercapacitor hybrid tramway. *J. Power Sources* **2015**, *279*, 267–280. [CrossRef]
5. Fagundes, T.A.; Fuzato, G.H.F.; Ferreira, P.G.B.; Biczkowski, M.; Machado, R.Q. Fuzzy Controller for Energy Management and SoC Equalization in DC Microgrids Powered by Fuel Cell and Energy Storage Units. *IEEE J. Emerg. Sel. Top. Ind. Electron.* **2022**, *3*, 90–100. [CrossRef]
6. Aguiar, C.R.D.; Fuzato, G.H.F.; Machado, R.Q.; Guerrero, J.M. An Adaptive Power Sharing Control for Management of DC Microgrids Powered by Fuel Cell and Storage System. *IEEE Trans. Ind. Electron.* **2020**, *67*, 3726–3735. [CrossRef]
7. Liu, Y.; Hu, Y.; Wang, Y.; Chau, T.K.; Zhang, X.; Iu, H.H.C.; Fernando, T. A Novel Adaptive Model Predictive Control for Proton Exchange Membrane Fuel Cell in DC Microgrids. *IEEE Trans. Smart Grid* **2022**, *13*, 1801–1812. [CrossRef]
8. Dinh, T.X.; Thuy, L.K.; Tien, N.T.; Dang, T.D.; Ho, C.M.; Truong, H.V.A.; Dao, H.V.; Do, T.C.; Ahn, K.K. Modeling and Energy Management Strategy in Energetic Macroscopic Representation for a Fuel Cell Hybrid Electric Vehicle. *J. Drive Control* **2019**, *16*, 11.
9. Li, H.; Ravey, A.; N'Diaye, A.; Djerdir, A. A novel equivalent consumption minimization strategy for hybrid electric vehicle powered by fuel cell, battery and supercapacitor. *J. Power Sources* **2018**, *395*, 262–270. [CrossRef]
10. Fu, Z.; Li, Z.; Si, P.; Tao, F. A hierarchical energy management strategy for fuel cell/battery/supercapacitor hybrid electric vehicles. *Int. J. Hydrogen Energy* **2019**, *44*, 22146–22159. [CrossRef]
11. Dang, T.D.; Do, T.C.; Truong, H.V.A.; Ho, C.M.; Dao, H.V.; Xiao, Y.Y.; Jeong, E.; Ahn, K.K. Design, Modeling and Analysis of a PEM Fuel Cell Excavator with Supercapacitor/Battery Hybrid Power Source. *J. Drive Control* **2019**, *16*, 45–53.
12. Li, T.; Liu, H.; Zhao, D.; Wang, L. Design and analysis of a fuel cell supercapacitor hybrid construction vehicle. *Int. J. Hydrogen Energy* **2016**, *41*, 12307–12319. [CrossRef]
13. Peng, F.; Zhao, Y.; Li, X.; Liu, Z.; Chen, W.; Liu, Y.; Zhou, D. Development of master-slave energy management strategy based on fuzzy logic hysteresis state machine and differential power processing compensation for a PEMFC-LIB-SC hybrid tramway. *Appl. Energy* **2017**, *206*, 346–363. [CrossRef]
14. Piraino, F.; Fragiacomo, P. A multi-method control strategy for numerically testing a fuel cell-battery-supercapacitor tramway. *Energy Convers. Manag.* **2020**, *225*, 113481. [CrossRef]
15. Trinh, H.-A.; Truong, H.-V.-A.; Ahn, K.K. Development of Fuzzy-Adaptive Control Based Energy Management Strategy for PEM Fuel Cell Hybrid Tramway System. *Appl. Sci.* **2022**, *12*, 3880. [CrossRef]
16. Wang, Y.; Sun, Z.; Chen, Z. Development of energy management system based on a rule-based power distribution strategy for hybrid power sources. *Energy* **2019**, *175*, 1055–1066. [CrossRef]
17. Marzougui, H.; Amari, M.; Kadri, A.; Bacha, F.; Ghouili, J. Energy management of fuel cell/battery/ultracapacitor in electrical hybrid vehicle. *Int. J. Hydrogen Energy* **2017**, *42*, 8857–8869. [CrossRef]
18. Xun, Q.; Lundberg, S.; Liu, Y. Design and experimental verification of a fuel cell/supercapacitor passive configuration for a light vehicle. *J. Energy Storage* **2021**, *33*, 102110. [CrossRef]
19. Wang, Y.; Sun, Z.; Chen, Z. Energy management strategy for battery/supercapacitor/fuel cell hybrid source vehicles based on finite state machine. *Appl. Energy* **2019**, *254*, 113707. [CrossRef]
20. Kaya, K.; Hames, Y. Two new control strategies: For hydrogen fuel saving and extend the life cycle in the hydrogen fuel cell vehicles. *Int. J. Hydrogen Energy* **2019**, *44*, 18967–18980. [CrossRef]
21. Do, T.C.; Truong, H.V.A.; Dao, H.V.; Ho, C.M.; To, X.D.; Dang, T.D.; Ahn, K.K. Energy Management Strategy of a PEM Fuel Cell Excavator with a Supercapacitor/Battery Hybrid Power Source. *Energies* **2019**, *12*, 4362. [CrossRef]
22. Li, Q.; Yang, H.; Han, Y.; Li, M.; Chen, W. A state machine strategy based on droop control for an energy management system of PEMFC-battery-supercapacitor hybrid tramway. *Int. J. Hydrogen Energy* **2016**, *41*, 16148–16159. [CrossRef]
23. Li, Q.; Wang, T.; Dai, C.; Chen, W.; Ma, L. Power Management Strategy Based on Adaptive Droop Control for a Fuel Cell-Battery-Supercapacitor Hybrid Tramway. *IEEE Trans. Veh. Technol.* **2018**, *67*, 5658–5670. [CrossRef]
24. Yedavalli, K.; Guo, L.; Zinger, D.S. Simple Control System for a Switcher Locomotive Hybrid Fuel Cell Power System. *IEEE Trans. Ind. Appl.* **2011**, *47*, 2384–2390. [CrossRef]

25. Garcia, P.; Fernandez, L.M.; Garcia, C.A.; Jurado, F. Energy Management System of Fuel-Cell-Battery Hybrid Tramway. *IEEE Trans. Ind. Electron.* **2010**, *57*, 4013–4023. [CrossRef]
26. García, P.; Fernández, L.M.; Torreglosa, J.P.; Jurado, F. Operation mode control of a hybrid power system based on fuel cell/battery/ultracapacitor for an electric tramway. *Comput. Electr. Eng.* **2013**, *39*, 1993–2004. [CrossRef]
27. Marzougui, H.; Kadri, A.; Martin, J.-P.; Amari, M.; Pierfederici, S.; Bacha, F. Implementation of energy management strategy of hybrid power source for electrical vehicle. *Energy Convers. Manag.* **2019**, *195*, 830–843. [CrossRef]
28. Zandi, M.; Payman, A.; Martin, J.; Pierfederici, S.; Davat, B.; Meibody-Tabar, F. Energy Management of a Fuel Cell/Supercapacitor/Battery Power Source for Electric Vehicular Applications. *IEEE Trans. Veh. Technol.* **2011**, *60*, 433–443. [CrossRef]
29. Hemi, H.; Ghouili, J.; Cheriti, A. A real time fuzzy logic power management strategy for a fuel cell vehicle. *Energy Convers. Manag.* **2014**, *80*, 63–70. [CrossRef]
30. Ameu, K.; Hadjaissa, A.; Cheikh, M.S.A.; Cheknane, A.; Essounbouli, N. Fuzzy energy management of hybrid renewable power system with the aim to extend component lifetime. *Int. J. Energy Res.* **2017**, *41*, 1867–1879. [CrossRef]
31. Ahmadi, S.; Bathaee, S.M.T.; Hosseinpour, A.H. Improving fuel economy and performance of a fuel-cell hybrid electric vehicle (fuel-cell, battery, and ultra-capacitor) using optimized energy management strategy. *Energy Convers. Manag.* **2018**, *160*, 74–84. [CrossRef]
32. Truong, H.V.A.; Dao, H.V.; Do, T.C.; Ho, C.M.; To, X.D.; Dang, T.D.; Ahn, K.K. Mapping Fuzzy Energy Management Strategy for PEM Fuel Cell–Battery–Supercapacitor Hybrid Excavator. *Energies* **2020**, *13*, 3387. [CrossRef]
33. Dao, H.V.; To, X.D.; Truong, H.V.A.; Do, T.C.; Ho, C.M.; Dang, T.D.; Ahn, K.K. Optimization-Based Fuzzy Energy Management Strategy for PEM Fuel Cell/Battery/Supercapacitor Hybrid Construction Excavator. *Int. J. Precis. Eng. Manuf. Green Technol.* **2021**, *8*, 1267–1285. [CrossRef]
34. Tao, F.; Zhu, L.; Fu, Z.; Si, P.; Sun, L. Frequency Decoupling-Based Energy Management Strategy for Fuel Cell/Battery/Ultracapacitor Hybrid Vehicle Using Fuzzy Control Method. *IEEE Access* **2020**, *8*, 166491–166502. [CrossRef]
35. Snoussi, J.; Elghali, S.B.; Benbouzid, M.; Mimouni, M.F. Optimal Sizing of Energy Storage Systems Using Frequency-Separation-Based Energy Management for Fuel Cell Hybrid Electric Vehicles. *IEEE Trans. Veh. Technol.* **2018**, *67*, 9337–9346. [CrossRef]
36. Snoussi, J.; Ben Elghali, S.; Benbouzid, M.; Mimouni, M.F. Auto-Adaptive Filtering-Based Energy Management Strategy for Fuel Cell Hybrid Electric Vehicles. *Energies* **2018**, *11*, 2118. [CrossRef]
37. Trinh, H.A.; Truong, H.V.A.; Ahn, K.K. Energy management strategy for fuel cell hybrid power system using fuzzy logic and frequency decoupling methods. In Proceedings of the 2021 24th International Conference on Mechatronics Technology (ICMT), Singapore, 18–22 December 2021; pp. 1–6.
38. Tremblay, O.; Dessaint, L.A. A generic fuel cell model for the simulation of fuel cell vehicles. In Proceedings of the 2009 IEEE Vehicle Power and Propulsion Conference, Dearborn, MI, USA, 7–10 September 2009; pp. 1722–1729.
39. Tremblay, O.; Dessaint, L.; Dekkiche, A. A Generic Battery Model for the Dynamic Simulation of Hybrid Electric Vehicles. In Proceedings of the 2007 IEEE Vehicle Power and Propulsion Conference, Arlington, TX, USA, 9–12 September 2007; pp. 284–289.
40. Oldham, K.B. A Gouy–Chapman–Stern model of the double layer at a (metal)/(ionic liquid) interface. *J. Electroanal. Chem.* **2008**, *613*, 131–138. [CrossRef]
41. Xu, N.; Riley, J. Nonlinear analysis of a classical system: The double-layer capacitor. *Electrochem. Commun.* **2011**, *13*, 1077–1081. [CrossRef]
42. Motapon, S.N.; Dessaint, L.; Al-Haddad, K. A Comparative Study of Energy Management Schemes for a Fuel-Cell Hybrid Emergency Power System of More-Electric Aircraft. *IEEE Trans. Ind. Electron.* **2014**, *61*, 1320–1334. [CrossRef]
43. Kollimalla, S.K.; Mishra, M.K.; Ukil, A.; Gooi, H.B. DC Grid Voltage Regulation Using New HESS Control Strategy. *IEEE Trans. Sustain. Energy* **2017**, *8*, 772–781. [CrossRef]
44. Erickson, R.W.; Maksimović, D. *Fundamentals of Power Electronics*, 3rd ed.; Springer: Berlin/Heidelberg, Germany, 2020.